

Controller Design, Analysis, and Experimental Validation of a Robotic Serpentine Tail to Maneuver and Stabilize a Quadrupedal Robot

William S. Rone

United States Air Force,
Eglin AFB, FL 32542
e-mail: wsrone@vt.edu

Wael Saab

SoftWear Automation, Inc.,
Atlanta, GA 30318
e-mail: waelsaab@vt.edu

Anil Kumar

GM Cruise, LLC,
San Francisco, CA 94103
e-mail: anilks@vt.edu

Pinhas Ben-Tzvi¹

Mem. ASME
Robotics and Mechatronics Laboratory,
Department of Mechanical Engineering,
Virginia Tech,
Blacksburg, VA 24061
e-mail: bentzvi@vt.edu

This paper analyzes how a multisegment, articulated serpentine tail can enhance the maneuvering and stability of a quadrupedal robot. A persistent challenge in legged robots is the need to account for propulsion, maneuvering, and stabilization considerations when generating control inputs for multidegree-of-freedom spatial legs. Looking to nature, many animals offset some of this required functionality to their tails to reduce the required action by their legs. By including a robotic tail on-board a legged robot, the gravitational and inertial loading of the tail can be utilized to provide for the robot's maneuverability and stability, while the legs primarily provide the robot's propulsion. System designs for the articulated serpentine tail and quadrupedal platform are presented, along with the dynamic models used to represent these systems. Outer-loop controllers that implement the desired maneuvering and stabilizing behaviors are discussed, along with an inner-loop controller that maps the desired tail trajectory into motor torque commands for the tail. Case studies showing the tail's ability to modify yaw-angle heading during locomotion (maneuvering) and to reject a destabilizing external disturbance in the roll direction (stabilization) are considered. Simulation results utilizing the tail's dynamic model and experimental results utilizing the tail prototype, in conjunction with the simulated quadrupedal platform, are generated. Successful maneuvering and stabilization are demonstrated by the simulated results and validated through experimentation. [DOI: 10.1115/1.4042948]

1 Introduction

In nature, animals rely on their tails to aid a variety of locomotive functions. Quadrupedal animals in particular utilize their tail for enhanced maneuvering and stabilization. For maneuvering, cheetahs use their tails to assist in turning [1] and geckos use their tails to re-orient in midair [2]. For stabilization, cats use their tail as an active counterbalance [3], kangaroos use their tail as an additional leg support during low-speed walking [4] and dinosaurs used their tail in a tripod-like stance to lift their front legs [5]. In all cases, the tail provides a mechanism separate from the legs' ground contact to impact the dynamics of the robot—a beneficial feature in unstructured environments in which leg ground contact cannot always be guaranteed.

However, bioinspired and biomimetic designs of legged robots typically omit robotic tails in favor of solely utilizing the legs for propulsion, maneuvering, and stabilization. In quadrupedal robots, this necessitates four spatial legs with a minimum of three active degrees-of-freedom (DOF), resulting in systems with at least 12DOF. These DOFs must then be controlled by sophisticated algorithms that simultaneously produce propulsion, maneuvering, and stability. Furthermore, loss of ground contact severely hampers the robot's ability to stabilize, as the ground contact loading at the feet is what stabilizes the system.

This research proposes utilizing a spatial, articulated tail to offset some of the required leg complexity into a single additional appendage. Figure 1 illustrates the tailed-quadruped system that is

considered in this analysis. A quadruped constructed from four robotic modular leg (RMLeg) [6] units is used as the legged robot subsystem, and the roll-revolute-revolute robotic tail (R3RT) is used as the articulated tail subsystem [7]. Each RMLeg is a 2DOF planar mechanism that is used to generate propulsion; the tail is used to generate the loading to provide maneuverability and enhance the quadruped's inherent stability.

This paper is organized as follows: Sec. 2 outlines prior work in both robotic tails and hyperredundant robot control. Section 3 describes the robotic tail subsystem design and model. Section 4 defines the outer- and inner-loop control laws used to implement the desired maneuvering and stabilization behaviors. Section 5 describes the quadruped subsystem design, gait planning, and modeling. Section 6 presents the simulation results for the

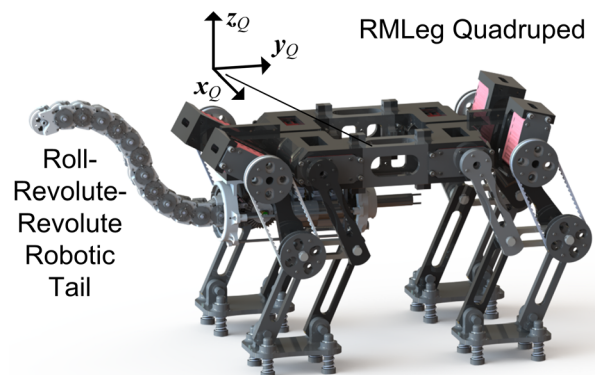


Fig. 1 RMLeg quadruped with an attached R3RT mechanism

¹Corresponding author.

Contributed by the Dynamic Systems Division of ASME for publication in the JOURNAL OF DYNAMIC SYSTEMS, MEASUREMENT, AND CONTROL. Manuscript received November 10, 2017; final manuscript received February 14, 2019; published online March 25, 2019. Assoc. Editor: Chuanfeng Wang.

maneuvering and stabilization case studies, and Sec. 7 presents results generated with experimentally measured tail loading. Section 8 concludes the paper and highlights planned future work.

2 Background

This section provides an overview of prior work in the fields of robotic tails (Sec. 2.1) and hyperredundant robot control (Sec. 2.2).

2.1 Robotic Tails. The dominant paradigm for robotic tails in the literature is single-mass, pendulum-like tails operating with 1DOF or 2DOF [8]. The 1DOF tails can operate in the pitch [9–11], yaw [12,13] or roll [14] directions and the 2DOF tails can operate in a combination of these two planes, such as pitch-yaw [15,16], yaw-pitch [17], and roll-pitch [18].

Prior single-DOF pendulum-like robotic tails may also be categorized based on their functional use on-board a mobile robot. In terms of propulsion, tails have been used to actuate walking [12] and rapidly accelerate or decelerate [9]. In terms of maneuvering, tails have been used for yaw-angle steering [13,14] and aerial re-orientation [16]. In terms of stabilization, tails have been used for disturbance rejection [18], center-of-mass (COM) adjustment [17], and dampening undesired ground contact [11].

Many of these applications draw their inspiration from the animals described in Sec. 1. However, in order to justify the addition of a tail to a legged robot, even if that tail reduces the required complexity in leg design and leg control, the tail must provide multiple functionalities for the system. Prior research into multifunctional tails is more limited than those focusing on a single use; prior multifunctional tail analyses include considerations for propulsion and maneuvering [15], as well as maneuvering and stabilization [10].

Articulated robot tail structures have also been studied. Three approaches for this class of tail include the roll–revolute–revolute robotic tail [7], the universal-spatial robotic tail [19,20], and the discrete modular serpentine tail [21]. In addition to these novel design concepts, preliminary studies have been presented into the control of these structures to realize maneuvering and stabilization behaviors [22,23]. Of particular importance are results from Ref. [7] which demonstrate the significant improvements serpentine tails offer over pendulum-like tails in terms of generating loading which positively impacts the system dynamics.

2.2 Hyperredundant Robot Control. Hyperredundant robots are systems that have a significantly higher number of joints than task space coordinates. If these joints are conventional discrete joints (such as revolute or universal joints), a hyperredundant robot is also called a serpentine robot. If the robot is instead defined by the continuous deformation of an elastic structure (such as a spring-steel backbone or pneumatic core), a hyperredundant robot is also called a continuum robot.

Although a serpentine structure was chosen for the proposed system’s robotic tail, the existing literature on serpentine robots primarily focuses on ground-supported snake-like robots and controllers designed to implement locomotion patterns. Furthermore, much of the prior work associated with continuum robot control focuses on cantilevered structures operating as manipulators. Although the R3RT is not used a robotic manipulator in this research, many of the same guiding principles apply.

Hyperredundant robot controllers are primarily differentiated by whether or not they utilize a robot model in the control formulation. Prior work into controllers that do not use a system model include proportional–integral–derivative (PID)-based approaches and neural-network-based approaches. Examples of PID-based controllers include individual joint controllers [24] and a proportional–derivative–controller acting based on segment curvatures [25]. Neural-network-based controllers utilize online tuning of the neural network during operation of the robot, as either a

standalone controller [26] or as a feedforward contribution to a controller that also employs a model-free nonlinear feedback loop [27]. This approach is particularly beneficial for continuum-type robots for which the robot’s continuous deformation presents a challenge for state modeling.

Model-based approaches augment aspects of the model-free approaches (specifically, PID-based control terms) with additional considerations for the modeled kinematics and/or dynamics of the robot. Prior work has utilized the robots’ Jacobians to map task-space sensor data into the joint-space in real-time [28–30], and dynamics-based controllers for vibration dampening have also been demonstrated [31].

3 Tail Subsystem

This section describes the structure of the serpentine tail under consideration for this analysis (Sec. 3.1), its associated dynamic model (Sec. 3.2) and the sensing incorporated into the design (Sec. 3.3).

3.1 Tail Design. Figure 2 shows the R3RT used as the tail subsystem for this analysis. The R3RT consists of a rigid housing, an actuation module, and two quasi-independently actuated tail segments each consisting of six links. The rigid housing connects to the quadruped subsystem and provides support for two coaxial bearings in which the actuation module is mounted. A slip ring is incorporated into the rigid housing that accommodates all of the wiring (power and communication) required for the actuation module, allowing for continuous roll rotation of the actuation module relative to the rigid housing.

The actuation module contains the three gearmotors (100 W Brushless DC Maxon motors with 15:1 reduction Maxon gearheads) used to actuate the R3RT. For the roll DOF, a spur gear/internal gear pair (3:1 reduction) is mounted between the roll-DOF gearmotor and rigid housing. For the two segments’ bending DOFs, a bevel gear pair (2:1 reduction) is mounted between the two gearmotors and their associated cable spool. A microcontroller and 3 motor drivers are also incorporated into the actuation module to operate the motors in torque control mode.

The articulated tail structure consists of 12 links serially connected to one another and the actuation module through parallel revolute pitch joints. Two actuated segments are created by two pairs of cables that route along the links: the first segment is created by terminating a cable pair at link 6, and the second segment is created by terminating a cable pair at link 12. Five equal-pitch gear pairs within each segment ensure the six relative joint angles in that segment are equal, and cable routing along nested cylindrical surfaces ensures that cable displacements are equal and opposite, allowing a single spool to drive each cable pair. The segments’ actuation is decoupled by utilizing an S-curve cable routing path for the segment 2 cabling through segment 1. Additional detail on the design of the R3RT can be found in Ref. [7].

3.2 Tail Model. The R3RT’s kinematic state may be represented by three variables: the roll angle φ and the segments 1 and

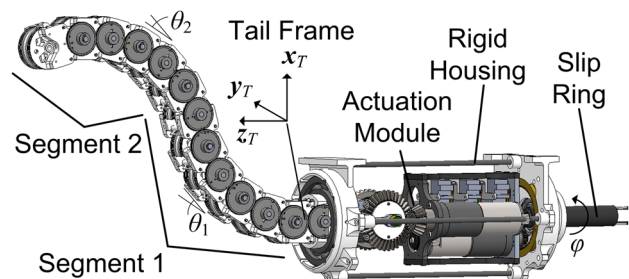


Fig. 2 R3RT subsystem design

2 relative joint angles θ_1 and θ_2 . Only two relative joint angles are needed to represent the state of the 12DOF tail structure due to the ten kinematic constraints imposed by the ten gear pairs. These state variables are collected into the state vector $\mathbf{q} = [\varphi, \theta_1, \theta_2]^T$.

The three control inputs for the R3RT are the actuation module torque τ_0 , the segment 1 spool torque τ_1 , and the segment 2 spool torque τ_2 . These input torques are collected into the control input vector $\mathbf{u} = [\tau_0, \tau_1, \tau_2]^T$.

The tail's dynamic equations of motion can be organized into the form shown in Eq. (1), where $\mathbf{M}(\mathbf{q})$ is the inertia matrix, $\mathbf{C}(\mathbf{q}, \dot{\mathbf{q}})\dot{\mathbf{q}}$ is the tail's centripetal and Coriolis loading effects, $\mathbf{g}(\mathbf{q})$ is the tail's gravitational loading, and \mathbf{T} is the actuation transmission matrix

$$\mathbf{M}(\mathbf{q})\ddot{\mathbf{q}} + \mathbf{C}(\mathbf{q}, \dot{\mathbf{q}})\dot{\mathbf{q}} + \mathbf{g}(\mathbf{q}) = \mathbf{T}\mathbf{u} \quad (1)$$

These equations are constructed by calculating the net moment at each joint due to the inertial and gravitational loading effects acting downstream of the joint (i.e., on links $j \geq i$ for joint i) and the gearing and actuation loading effects acting across the joint (i.e., coaxial force pairs acting on bodies separated by joint i). The component of this net joint moment aligned with the joint's revolute axis of rotation is prescribed to be zero, as a revolute joint cannot support a moment about its axis. These 13 equations are a set of differential-algebraic equations defined by three differential variables (\mathbf{q}) and ten algebraic variables (the gear pairs' contact forces). Algebraic manipulation can be used to reduce these 13 differential-algebraic equations into the three ordinary differential equations defined by Eq. (1).

The actuation transmission matrix accounts for the transmission of the actuation along the tail. If friction is neglected, it is a constant matrix due to the geometric similarity of the 12 serpentine links. In this analysis, friction is not accounted for within the dynamic model, but an empirical friction correction is added to the calculated motor inputs in Sec. 7.

Detailed formulations for the dynamics of the R3RT can be found in Ref. [7].

3.3 Tail Sensing. The sensing incorporated into the tail measures the roll and spool angles and estimates tail motor speeds during operation. Roll and spool angles are measured by absolute encoders (U.S. Digital MA3-P10-125-N) coupled between the rigid housing and actuation module (for the roll angle) and between the actuation module and spool (for the spool angles). Motor speeds are estimated utilizing incremental encoders (U.S. Digital E4T-360-236-DHMB) mounted on the gearmotor rotor's rear shaft.

4 Tail Control

Figure 3 illustrates the controller used to operate the tailed-quadraped. Outer-loop control laws (Sec. 4.1) plan desired tail

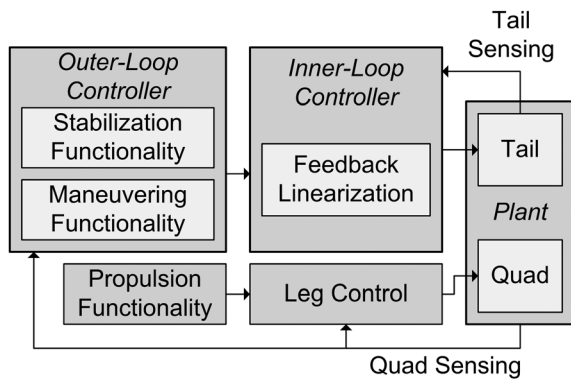


Fig. 3 Tailed-quadraped control concept

trajectories designed to implement maneuvering and stabilization behaviors in the system, and an inner-loop control law (Sec. 4.2) is designed to calculate the $\mathbf{u}(t)$ trajectory needed to implement the desired tail state trajectory.

4.1 Outer-Loop Control. Two outer-loop controllers are considered in this analysis: a maneuvering controller capable of generating yaw-angle displacements of the tailed-quadraped during locomotion, and a stabilizing controller capable of preventing the quadraped from rolling over due to a destabilizing disturbance.

4.1.1 Maneuvering Control. The maneuvering controller in this case study will generate a dynamic tail motion designed to change the heading angle of the robot without destabilizing locomotion. Although this functionality has been studied in various forms in previous work [7,22,23], a novel method of trajectory planning is considered here to regulate motor torque throughout the tail trajectory and improve motor power output by prescribing greater angular accelerations when angular velocity is low, and lower angular accelerations when angular velocity is high.

In this approach, the two segments' joint angles are prescribed to be equal ($\theta = \theta_1 = \theta_2$), and the joint angle trajectories are defined based on a prescribed profile for the product $\dot{\theta}\ddot{\theta}$ between the angular velocity $\dot{\theta}$ and acceleration $\ddot{\theta}$, shown in Fig. 4. This product is a kinematic analog to the motor's power output, as there is a direct relationship between angular acceleration and motor torque.

From t_0 to t_A , the product increases from zero to the value $\dot{\theta}(t_A)\ddot{\theta}_n$, where $\ddot{\theta}_n$ is the peak joint angle acceleration. In this phase, due to the low $\dot{\theta}$, a profile for $\ddot{\theta}$ is prescribed using Eq. (2) instead of dividing a desired $\dot{\theta}\ddot{\theta}$ trajectory in this time span by $\dot{\theta}$

$$\ddot{\theta}(t) = \begin{cases} \ddot{\theta}_n \frac{t - t_0}{(t_A - t_0)/2} & \text{if } t_0 \leq t \leq \frac{1}{2}(t_0 + t_A) \\ \ddot{\theta}_n & \text{if } \frac{1}{2}(t_0 + t_A) < t \leq t_A \end{cases} \quad (2)$$

From t_A to t_B , $\dot{\theta}\ddot{\theta}(t)$ is defined to maintain a constant product of $\dot{\theta}\ddot{\theta} = \dot{\theta}_A\ddot{\theta}_n = \eta$ as defined in Eq. (3), where $\dot{\theta}_A = \dot{\theta}(t_A)$. From t_B to t_1 , the defined $\ddot{\theta}$ is linearly scaled to zero to ensure $\ddot{\theta}_1 = 0$

$$\ddot{\theta}(t) = \begin{cases} \frac{\eta}{\dot{\theta}} & \text{if } t_A < t \leq t_B \\ \frac{\eta}{\dot{\theta}} \frac{t_1 - t}{t_1 - t_B} & \text{if } t_B < t \leq t_1 \end{cases} \quad (3)$$

Equation (4) defines the trajectory from t_1 to t_2 , which is the mirror opposite of the $\dot{\theta}$ trajectory from t_0 to t_1

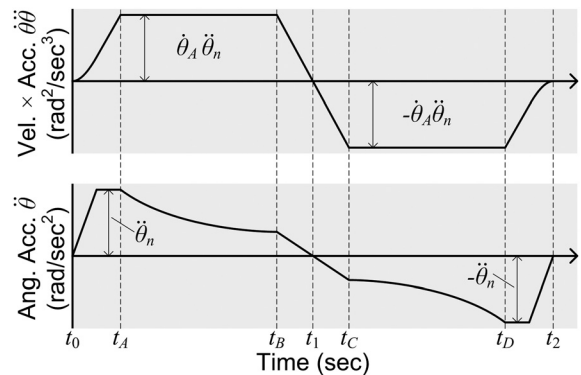


Fig. 4 Desired trajectories for joint velocity/acceleration product and joint acceleration

$$\ddot{\theta}(t) = \begin{cases} -\frac{\eta}{\theta} \frac{t-t_1}{t_c-t_1} & \text{if } t_1 < t \leq t_c \\ -\frac{\eta}{\theta} & \text{if } t_c < t \leq t_D \\ -\ddot{\theta}_n & \text{if } t_D < t \leq \frac{1}{2}(t_D+t_2) \\ -\ddot{\theta}_n \frac{t_2-t}{(t_2-t_D)/2} & \text{if } \frac{1}{2}(t_D+t_2) < t \leq t_2 \end{cases} \quad (4)$$

The desired $\dot{\theta}(t)$ and $\theta(t)$ trajectories are found by integrating the defined $\ddot{\theta}$ trajectory once and twice from the initial conditions $\dot{\theta}_0$ and θ_0 . From these bending angle trajectories, a desired state trajectory \mathbf{q}_d and its derivatives $\dot{\mathbf{q}}_d$ and $\ddot{\mathbf{q}}_d$ may be calculated by setting $\varphi = \pi/2$.

For fixed time span parameters, there is a functional relationship between the joint angle displacement $\Delta\theta = \theta_2 - \theta_0$ and $\ddot{\theta}_n$ (i.e., $\Delta\theta = f_n(\ddot{\theta}_n)$). Simulations over a range of $\ddot{\theta}_n$ values can be used to characterize this functional relationship, and inverting it allows for a $\ddot{\theta}_n$ value to be selected to implement the desired change in heading angle, similar to the single-tail motion analysis in Ref. [23].

4.1.2 Stabilization Control. The stabilization controller in this case study will prescribe a tail motion that utilizes the tail's inertial and gravitational loading to counteract a destabilizing load applied to the quadruped. Based on the quadruped's geometry and mass distribution, the moment of inertia with respect to the roll axis y_Q is significantly lower than that of the pitch axis x_Q (axes defined in Fig. 1), making roll angle destabilization more likely for a lower magnitude disturbance. Therefore, the stabilization controller is designed to counteract a destabilizing moment about this roll axis.

Roll destabilization can be detected from the quadruped's roll angle ρ . During steady-state locomotion, slight variations in ρ are expected, and the range of acceptable roll angles without requiring tail intervention can be defined as $\rho \in [-\rho_b, \rho_b]$. Beyond these limits, the tail should be actuated to oppose the destabilizing roll influence. The required stabilizing tail actuation is parameterized by the variable $\kappa \in [-1, 1]$, defined in Eq. (5) and shown in Fig. 5, where ρ_{lim} is the roll angle magnitude beyond which $|\kappa| = 1$, "sat" is the unit saturation function, and "sgn" is the signum function. The $-\text{sgn}(\rho)$ term ensures that stabilizing control action acts in opposition to the quadruped's roll angle.

$$\kappa = \begin{cases} 0 & \text{if } |\rho| \leq \rho_b \\ \text{sat}\left(-\text{sgn}(\rho) \frac{|\rho| - \rho_b}{\rho_{lim} - \rho_b}\right) & \text{if } |\rho| > \rho_b \end{cases} \quad (5)$$

When $|\kappa| > 0$, a methodology for mapping κ into a second-order continuous tail trajectory is needed; the variable ψ is used to parameterize this continuous trajectory. A unit damped harmonic oscillator for ψ is defined in Eq. (6) with κ as its forcing function, where ξ and ω_n are the oscillator's damping ratio and natural frequency, respectively. To minimize the system's settling time without overshoot, ξ is set equal to 1, and ω_n is defined in Sec. 6

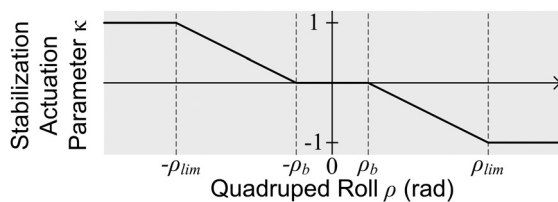


Fig. 5 Stabilization actuation parameter κ definition

$$\frac{1}{\omega_n^2} \ddot{\psi} + \frac{2\xi}{\omega_n} \dot{\psi} + \psi = \kappa, \quad \{\psi_0, \dot{\psi}_0\} = 0 \quad (6)$$

The ψ trajectory is used to continuously transition the tail state \mathbf{q} from its nominal tail configuration \mathbf{q}_0 during steady-state locomotion to the stabilization steady-state configuration \mathbf{q}_{st} , as defined in Eq. (7). The states \mathbf{q}_0 and \mathbf{q}_{st} are determined based on considerations for (1) symmetry, (2) gravity, and (3) conservation of angular momentum. To simplify analysis, $\theta_1 \geq 0$ to avoid equivalent tail states such as $\mathbf{q} = [0, \theta_1, \theta_2]^T = [180 \text{ deg}, -\theta_1, -\theta_2]^T$. In addition, the discussion below will assume $\rho > 0$; a parallel justification can be made for $\rho < 0$

$$\mathbf{q} = \mathbf{q}_0 + (\mathbf{q}_{st} - \mathbf{q}_0)\psi \quad (7)$$

First, based on symmetry, $\varphi_0 = \{0, \pm 180 \text{ deg}\}$ so that the tail can respond equivalently in either direction. Second, to maximize the gravitational loading at \mathbf{q}_{st} with respect to the roll axis, define $\mathbf{q}_{st} = [-90 \text{ deg}, 15 \text{ deg}, 0]^T$. Third, conservation of angular momentum dictates that the relative rotation $\varphi_{st} - \varphi_0$ should be the same sign as ρ to induce rotation in the opposite direction in the quadruped. Based on these conditions, $\mathbf{q}_0 = [-180 \text{ deg}, \theta_{1,0}, \theta_{2,0}]^T$ and $\mathbf{q}_{st} = [-90 \text{ deg}, 15 \text{ deg}, 0]^T$, with free choices of $\theta_{1,0}$ and $\theta_{2,0}$ based on other considerations. This analysis will define $(\theta_{1,0}, \theta_{2,0}) = (15 \text{ deg}, 0)$ to minimize the required tail motion during stabilization.

4.2 Inner-Loop Control. The inner-loop controller utilized in this analysis is a model-based feedback linearization controller that prescribes both feedforward inputs based on the modeled tail dynamics and feedback inputs based on the measured tail error.

Equation (8) defines the feedback linearizing controller. In this equation, $\hat{\mathbf{M}}$ denotes the estimate of the corresponding matrix or vector (in this case, \mathbf{M}) from Eq. (1), $\tilde{\mathbf{q}}$ is the error $\mathbf{q} - \mathbf{q}_d$ between the measured and desired states and \mathbf{K}_0 and \mathbf{K}_1 are outer-loop linear feedback gains. This analysis will assume that the estimate for a given matrix or vector matches the actual matrix or vector (i.e., $\hat{\mathbf{M}} = \mathbf{M}$); future work will consider potential modeling errors and the inclusion of additional control terms to compensate for these

$$\mathbf{u} = \hat{\mathbf{T}}^{-1} (\hat{\mathbf{M}}(\ddot{\mathbf{q}}_d - \mathbf{K}_0 \tilde{\mathbf{q}} - \mathbf{K}_1 \dot{\tilde{\mathbf{q}}}) + \hat{\mathbf{C}} \dot{\tilde{\mathbf{q}}} + \hat{\mathbf{g}}) \quad (8)$$

This controller leads to the closed-loop system dynamics shown in Eq. (9), which is canonically asymptotically stable if \mathbf{K}_0 and \mathbf{K}_1 are positive definite

$$\ddot{\tilde{\mathbf{q}}} + \mathbf{K}_1 \dot{\tilde{\mathbf{q}}} + \mathbf{K}_0 \tilde{\mathbf{q}} = 0 \quad (9)$$

5 Quadruped Subsystem

This section presents the quadruped design (Sec. 5.1) used in conjunction with the R3RT to study the tail's maneuvering and stabilization capabilities, along with the gait planning used to propel the quadruped (Sec. 5.2) and the quadruped's dynamic model (Sec. 5.3).

5.1 Quadruped Design. Figure 6(a) shows a side-view schematic diagram of the quadruped robot composed of four RMLeg units [6]. Each RMLeg is a 2DOF planar mechanism composed of two serially connected four-bar mechanisms analogous to a thigh and shin.

The two four-bar mechanisms have parallelogram topologies (opposite links have equal lengths), which results in double-rocker behavior. This behavior constrains the RMLeg's foot link orientation to remain parallel to the quadruped body link as the thigh and shin links move. This guarantees a parallel flat foot orientation with respect to the quadruped body without needing an

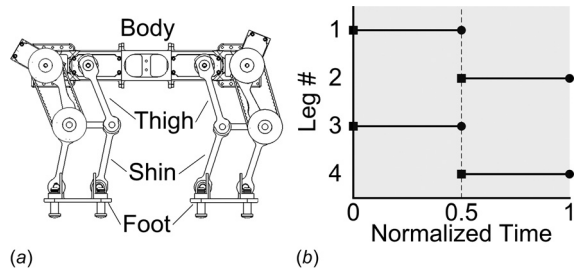


Fig. 6 (a) Side view schematic diagram of the quadruped subsystem and (b) gait diagram

additional actuator between the shin and foot links. On flat surfaces, flat feet provide a more stable support polygon compared to feet with a point or line contact.

One of the main benefits of using a four-bar mechanism is actuation decoupling. The thigh is actuated directly by a motor mounted within the quadruped body, and the shin is actuated by a motor mounted on one of the two thigh links. A 1:1 timing belt transmits the thigh motor actuation to the shin. Mounting the shin motor to the thigh instead of the hip allows this actuator to control the relative motion between the thigh and shin links and not have to compensate for the thigh actuation.

Four compliant toes are incorporated into the foot to help maintain planar contact between the foot and ground even when the quadruped's body is not parallel to the ground. Instead of tipping along one of the sides of the foot, the toes will extend and retract in response to the quadruped's pitch and rolling. However, once these toes reach their displacement limits, loss of ground contact for one or more toes (and possibly the foot) will occur.

5.2 Gait Planning. The quadruped robot is designed to provide forward locomotion in a single direction, with the tail capable of performing steering (maneuvering) and disturbance rejection (stabilization) functions. To realize a forward quasi-static walking gait, a trot gait pattern is utilized in which the legs alternate between a support phase, in which the foot is in contact with the ground, and a lift phase, in which it is airborne. The support phase foot trajectory is a straight line with constant velocity, and the lift phase is designed to raise the foot and move it in front of its hip for its next support phase.

Trot gaits provide quadrupeds with planar foot contact a quasi-statically stable walking gait if the quadruped's zero-moment point falls within the support polygon created by the geometric boundary created by all of the ground contact points at a given time. Figure 6(b) illustrates the gait diagram for this type of trotting. The plot's horizontal axis spans the normalized time for a single foot trajectory cycle. The line segment for each leg represents the support phase, from landing (square at start) to takeoff (circle at end). The quadruped alternates between diagonal pairs of legs in contact with the ground. Therefore, two support phase feet move cooperatively (i.e., in the same direction) for forward walking and the system zero-moment point can be configured such that it always falls within the support polygon.

5.3 Quadruped Dynamic Simulation. A three-dimensional computer-aided design model of the RMLeg quadruped was created in SOLIDWORKS and exported to MSC ADAMS, a multibody dynamic simulation software. This software enables a comprehensive simulation and motion analysis capable of solving for the kinematics and dynamics of the quadruped.

In addition to the system's inertial loading effects based on the imported computer-aided design mass properties and geometry, loading effects are incorporated into the model for the tail loading, gravity, and contact between the 16 toes and ground. The contact loading between the toes and ground are defined by setting stiffness, force exponent, damping and penetration depth, and the

associated friction is defined using a continuous velocity-dependent calculation of the friction coefficient. The desired leg trajectories are prescribed as kinematic constraints on the hip and knee joints of each leg and MSC ADAMS implicitly calculates the joint torques used to drive the associated joints.

MSC ADAMS/Control was used to export the plant simulation to a SIMULINK block with six inputs (three components each of tail force and moment) and four outputs (quadruped forward velocity and yaw/pitch/roll angles).

6 Simulation Results

This section interfaces the tail and quadruped models described in Secs. 3 and 5 and implements the controllers from Sec. 4 to analyze the tail's ability to maneuver (Sec. 6.2) and stabilize (Sec. 6.3) the tailed-quadruped system described in Sec. 6.1.

6.1 Simulation Parameters. For this analysis, the existing R3RT and RMLeg subsystem prototypes were used as the baseline for analysis. Specifically, the geometric, mass, and inertia properties of these prototypes in Refs. [6] and [19] were utilized, with modifications made as discussed below.

For the quadruped, the mass properties of the simulated system needed to match the loading capacity available for the existing robotic tail. To accomplish this, the mass of the quadruped frame and legs were scaled down to 30% of their nominal values to enable the tail to achieve meaningful yaw rotation with a single tail motion. Connectors were needed between the fore and aft pairs of legs to provide sufficient spacing for the feet, and an additional proof mass in the head was added to help balance the cantilevered tail. The nominal quadruped mass m_Q and body-frame inertia I_Q^O are defined in Eq. (10) at the quad COM. This inertia does change during locomotion due to the leg motion, but this is calculated and accounted for automatically by MSC ADAMS

$$m_Q = 4.876 \text{ kg}, \quad I_Q^O = \begin{bmatrix} 0.1723 & 0.0007 & -0.4 \\ 0.0007 & 0.4343 & 0.0001 \\ -0.4 & 0.0001 & 0.4291 \end{bmatrix} \text{ kg} \cdot \text{m}^2 \quad (10)$$

The quadruped's nominal gait during both simulations generate an average forward velocity of 750 mm/s with a step length of 250 mm (1.5 gait cycles per second) and a maximum foot lift of 50 mm.

For the tail, 1.4 kg is distributed along the tail length. The 12 links along the tail are 40 mm long, their COMs are modeled as 36 mm from their proximal revolute joint, and their cylindrical cable-routing surfaces are 50 mm in diameter.

6.2 Maneuvering Case Study. For the maneuvering case study, the loading generated by a single tail motion was applied to the quadruped during locomotion to observe the resulting quadruped yaw rotation.

During preliminary simulations for the maneuvering case study, it was found that the friction at the feet was a severely limiting factor for effective turning with a reasonable tail mass. With a dynamically stable gait, this challenge could be mitigated by choosing to actuate the tail during an airborne gait phase in which all legs are lifted from the ground. However, for the quasi-statically stable gait currently under consideration, at least two legs are in contact with the ground at all times.

To mimic an airborne gait phase in this analysis, a hop is added during the walking trajectory to lift the quadruped off the ground for 0.45 s and move the tail during this time. In addition, due to the absence of friction between the ground and quadruped during this time, the net rotation of the quadruped depends only on the net rotation of the tail and not the duration over which that motion occurs. However, this ground friction is beneficial when returning the tail from its bent configuration after maneuvering to its

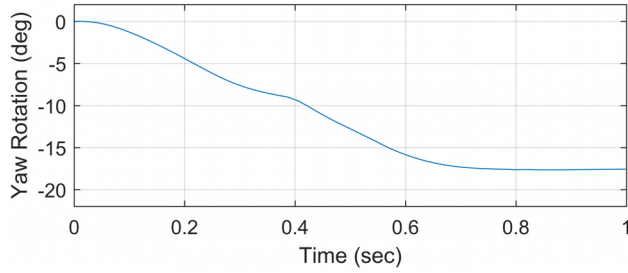


Fig. 7 Maneuvering case study yaw-angle rotation

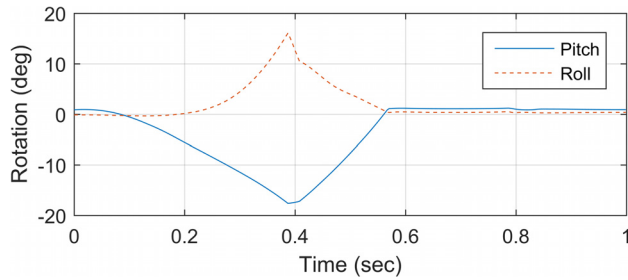


Fig. 8 Maneuvering case study pitch- and roll-angle trajectories

nominal configuration: if the system were airborne during this return, the generated yaw rotation would be undone.

Figure 7 illustrates the change in yaw-angle heading due to a tail bend of 90 deg in segments 1 and 2. Unlike the maneuvering results in Refs. [22] and [23], the heading angle magnitude monotonically increases. In those cases, friction acting against the desired motion of the quadruped caused the quadruped angular velocity to reach zero before the tail velocity reached zero during the tail's deceleration. Then, the tail's continuing deceleration induced an undesired rotation in the quadruped in the undesired direction. In this case, angular momentum between the tail and quadruped is conserved.

A key requirement of a robotic tail is that the loading generated by the tail does not induce instabilities in the DOFs orthogonal to the one under consideration. Figure 8 illustrates the associated pitch and roll angle trajectories of the quadruped due to the yawing tail motion. As shown, while the tail motion does induce slight undesired displacements in each, these do not cause destabilization.

Simulations were also generated for the case in which the tail segments bend from -90 deg to 90 deg while the quadruped is airborne. However, the auxiliary loading generated by the tail in the roll-direction induced instability.

Net changes to the quadruped's yaw heading angle in excess of the rotation that can be generated by a single tail motion may be generated by performing multiple tail motions in sequence. As discussed in Sec. 4.1.1, the functional relationship between $\ddot{\theta}_n$ and the net change in yaw-angle heading may be developed using simulations, to allow use of the multiple tail motion maneuvering algorithm described in Ref. [23].

6.3 Stabilization Case Study. For the stabilization case study, an impulsive moment of magnitude M_δ is applied for 0.2 s in the roll direction of the quadruped during locomotion. Without active tail control, depending on the magnitude of M_δ , one of three scenarios will occur.

- (1) The quadruped's gravitational loading will reject the disturbance without significant change in roll angle. This occurs in the range $M_\delta \in [0, 10.1]$ N·m, in which the quadruped's roll angle $|\rho|$ remains less than 3 deg. Thus, the

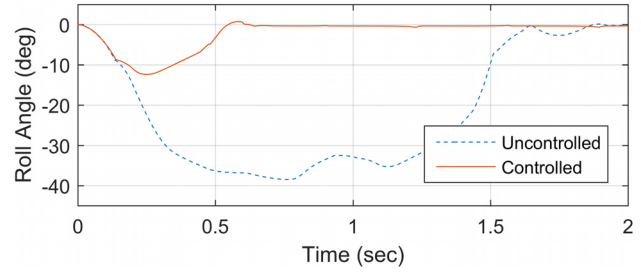


Fig. 9 Stabilization case study quadruped marginal stability with and without tail control action

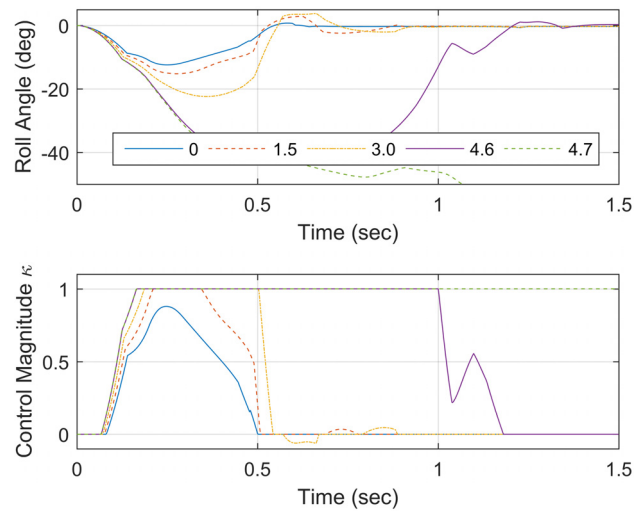


Fig. 10 Stabilization case study ρ and κ trajectories for varying disturbance magnitudes $M_\delta = M_{\delta,0} + M_{\delta,Q} + \Delta M$

moment disturbance threshold for nontrivial roll-angle variations is $M_{\delta,0} = 10.1$ N·m.

- (2) The quadruped will experience nontrivial roll displacement ($|\rho| > 3$ deg), but the disturbance is not sufficient to tip the quadruped and destabilize it. This occurs in the range $M_\delta \in [M_{\delta,0}, M_{\delta,0} + 15.5]$ N·m. Thus, the additional moment disturbance beyond $M_{\delta,0}$ the quadruped can accommodate without destabilizing is $M_{\delta,Q} = 15.5$ N·m.
- (3) The disturbance is sufficient to tip the quadruped and destabilize the system in the roll DOF. Without active stabilization, this occurs when $M_\delta > M_{\delta,0} + M_{\delta,Q}$. However, when the tail is used to actively stabilize the quadruped using the controller detailed in Sec. 4.1.2, a significant improvement in roll angle stability is observed.

The parameters used for the controller are defined in Eq. (11): no control action is taken for roll angle disturbances less than 3 deg, full control action is applied once the roll is greater than 13 deg, and the settling time of the tail position is $3\zeta/\omega_n = 0.15$ s

$$\rho_b = 3 \text{ deg}, \quad \rho_{\text{lim}} = 13 \text{ deg}, \quad \omega_n = 20 \text{ rad/s} \quad (11)$$

Figure 9 illustrates the roll-angle trajectory of the quadruped for a disturbance of magnitude $M_\delta = M_{\delta,0} + M_{\delta,Q}$. Active tail-based stabilization provided a 68% reduction in peak roll-angle in relation to the passive case, which allows the system to further accommodate additional disturbance loading.

Figure 10 illustrates the roll-angle ρ and control action parameter κ trajectories for disturbances of magnitude $M_\delta = M_{\delta,0} + M_{\delta,Q} + \Delta M$ for which $\Delta M \in \{0, 1.5, 3.0, 4.6, 4.7\}$ N·m. The maximum ΔM allowable before the tailed-quadruped destabilizes is $M_{\delta,T} = 4.6$ N·m, which represents a 30% improvement to $M_{\delta,Q}$.

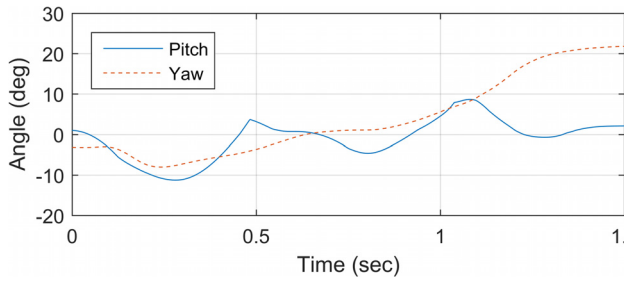


Fig. 11 Stabilization case study pitch and yaw-angle trajectories

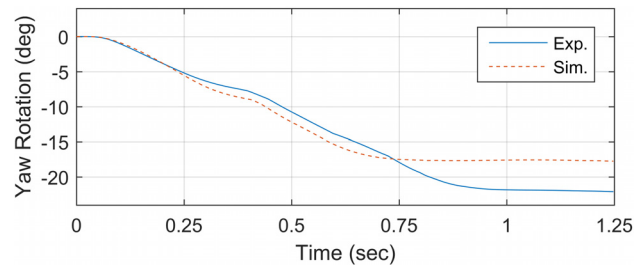


Fig. 14 Maneuvering case study simulated and experimental yaw angle trajectories

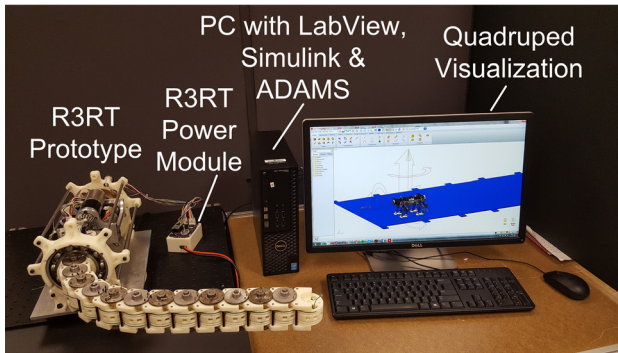


Fig. 12 Tail hardware-in-the-loop experimental setup

As with the maneuvering case, the roll-stabilizing control action should not destabilize the tailed-quadraped in the pitch or yaw directions. Figure 11 illustrates the system's pitch and yaw trajectories due to the stabilizing tail motion when $\mathbf{M}_\delta = \mathbf{M}_{\delta,0} + \mathbf{M}_{\delta,Q} + \mathbf{M}_{\delta,T}$. Although the tail does not destabilize the system in the pitch direction, it does result in a net nonzero yaw angle after the tail returns to its nominal configuration. This heading error can then be compensated for using an appropriately scaled maneuvering tail motion.

7 Experimental Results

This section utilizes the R3RT prototype in conjunction with the quadraped simulation to verify the simulation-based results in Sec. 6. The experimental setup is described (Sec. 7.1), and the maneuvering (Sec. 7.2) and stabilization (Sec. 7.3) case studies are considered with the tail prototype.

7.1 Experimental Setup. To augment the simulation-based studies detailed in Sec. 6, a series of hardware-in-the-loop simulations were conducted. Hardware-in-the-loop (HIL) simulations use real, physical system hardware to replace one or more simulated subsystems in an analysis. Although HIL simulations typically utilize a physical embedded system in conjunction with a mechanical plant simulation, the distinct mechanical subsystems of the tailed-quadraped lend themselves to this type of analysis. As a precursor to full-scale implementation of the tailed-quadraped in future work (Sec. 8), a prototype R3RT is used in conjunction with a simulated RMLeg quadraped walking in a virtual environment on flat terrain.

Figure 12 illustrates the experimental setup used in this section. The R3RT prototype is mounted on a six-axis load cell (Sunrise Instruments M3716B) to measure the force and moment generated by the tail, which is then mapped into the equivalent force and moment at the tail frame origin (this is the loading the simulated tail calculated).

Control inputs for the tail experiments were generated by recording the calculated control input trajectories $\mathbf{u}(t)$ and state vector accelerations $\ddot{\mathbf{q}}(t)$ during a simulation. Using dynamic models of the actuation transmission mechanisms between the roll DOF/spools and motors, these torques and accelerations were mapped into motor current commands. In addition, an empirical current offset was also added to overcome the friction within the actuation transmission mechanism and along the tail.

The functional performance of the R3RT in terms of maneuvering and stabilization is assessed in two ways. First, the loading calculated by the simulated R3RT is compared to the loading measured from the prototype R3RT. Second, the performance of the prototype tail in terms of maneuvering and stabilization is assessed using a HIL simulation.

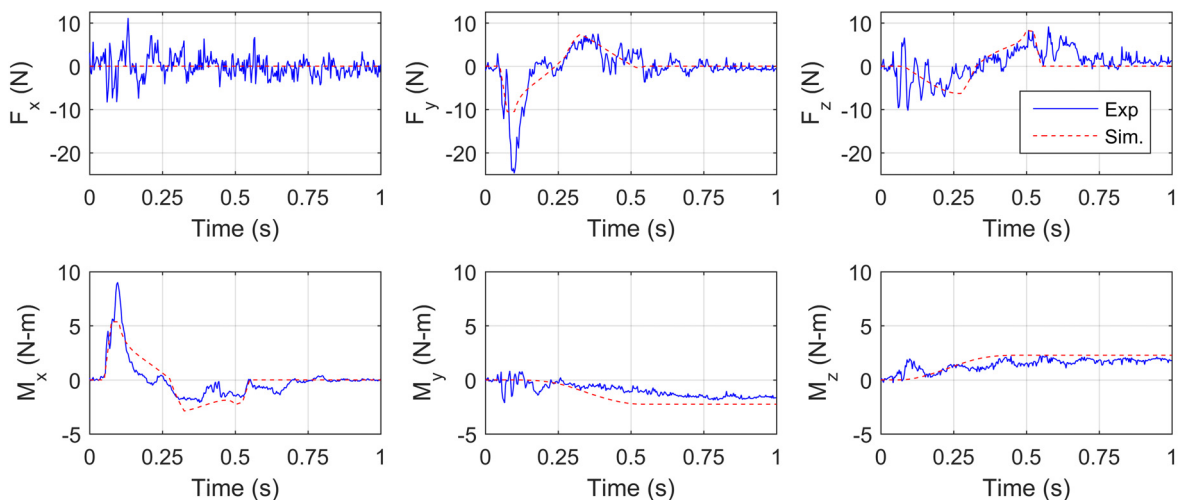


Fig. 13 Maneuvering case study simulated and experimental loading comparison

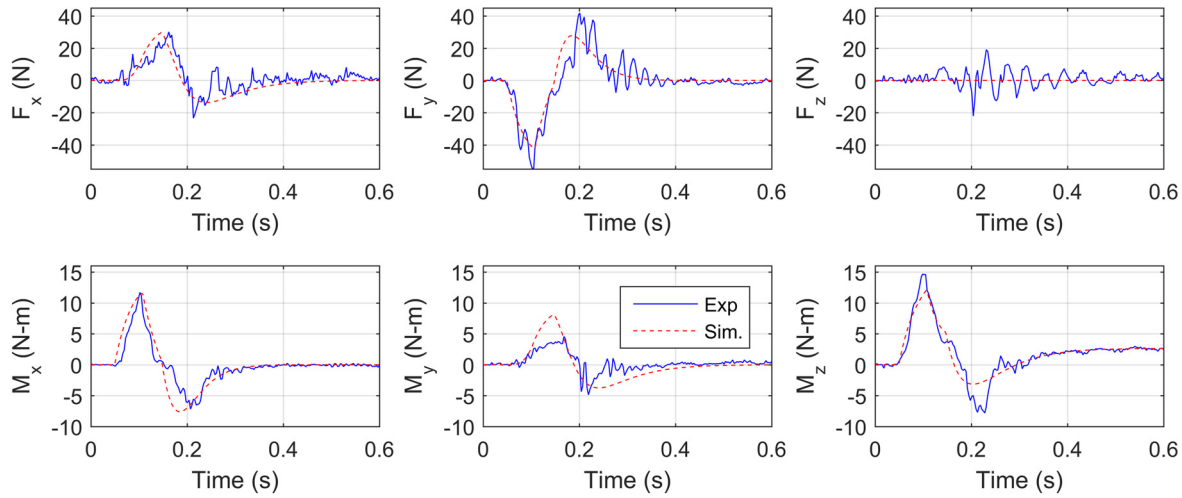


Fig. 15 Stabilization case study simulated and experimental loading comparison

7.2 Maneuvering Case Study. Figure 13 compares the simulated and experimentally measured loading generated by the maneuvering tail motion, and Fig. 14 compares the simulated yaw-angle rotation due to the simulated and experimentally measured loading. To reduce the noise in the experimentally measured trajectories, three experiments for each tail motion were performed and the resulting loading averaged together.

The x-component of moment is the most critical in this case study, and the increase in peak moment magnitude in the acceleration phase coupled with a lower magnitude moment and longer duration of the deceleration phase leads to the increased rotation observed in the yaw angle for the experimental loading case.

The feedback linearization inner-loop controller used to generate the motor torque inputs in this analysis also shows significant improvement in terms of lag time compared to the inner-loop velocity controller used in Ref. [7]. In that work, the initial peak loading was predicted to occur at 0.1 s, but the experimentally measured initial peak loading did not occur until 0.3 s. As shown in Fig. 13, the initial peak error is on the order of hundredths of a second, on par with the sampling rate.

The friction compensation current offsets required for bending the segments was significantly higher than anticipated, and likely resulted in shortcomings in the tracking of the desired dynamic trajectory. Future work will investigate methods to experimentally measure and model friction within the tail mechanism, allowing for more accurate control, particularly when coupled with tail models that more accurately model the dynamic friction behavior.

7.3 Stabilization Case Study. For this case study, the $u(t)$ and $\dot{q}(t)$ for the experimental trials were calculated for the case in which $M_\delta = M_{\delta,0} + M_{\delta,Q} + M_{\delta,T}$.

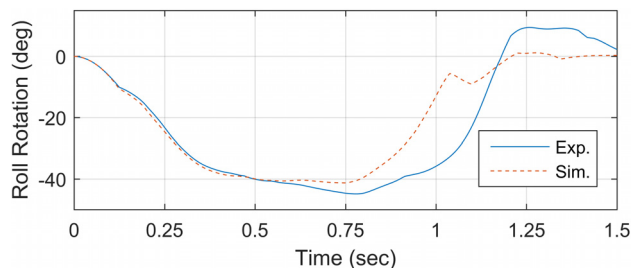


Fig. 16 Stabilization case study simulated and experimental yaw angle trajectories

Figure 15 compares the simulated and experimentally measured loading generated by the stabilizing tail motion, and Fig. 16 compares the simulated roll-angle rotation due to the simulated and experimentally measured loading. For the experimental loading HIL simulation, the magnitude of the disturbance was reduced by 0.1 N-m, as the system was unstable for the simulation's M_δ .

The z-component of moment is the most critical in this case study; like the stabilization case, the tail simulation underestimated the moment's maximum and minimum magnitudes, but the impact of this variation on the simulation's predicted performance of the robot is significantly less than the stabilization case. The simpler actuation transmission mechanism between the motor and roll DOF also required less friction compensation in relation to the bending tail motions, providing for a more accurate simulation of the tail behavior.

8 Conclusion

This paper has presented controllers designed to stabilize and maneuver a quadrupedal robot. Outer-loop control laws have been formulated for a yawing tail motion to turn the quadruped during locomotion and a rolling tail motion to improve external roll-DOF disturbance rejection during locomotion. An inner-loop controller maps the desired tail trajectories generated by these outer-loop controllers into tail inputs, and simulations have demonstrated their efficacy in conjunction with a simulated quadrupedal platform. Experiments utilizing the control inputs calculated for the simulations validate the simulated loading profiles generated by the tail and offer similar performance as observed from the HIL experiments.

Future work will focus on the coupled simulation of the tail and quadrupedal subsystems, as opposed to the segregated treatment discussed in this paper. This will transition the quadruped model from the MSC ADAMS-based simulation into the same simulation framework as the tail. Improvements to the tail's inner-loop controller will also be studied to account for possible variations between the simulated and experimental tail structures and to modify the actuation input calculation to robustly account for these uncertainties. The ultimate goal of this research is the full-scale integration of the tail prototype with a quadrupedal system to fully demonstrate the functionalities described herein.

Acknowledgment

The views expressed in this article do not necessarily represent the views of the Department of Defense and its components or the United States.

Funding Data

- The National Science Foundation (Grant No. 1557312; Funder ID: 10.13039/501100008982).

References

- [1] Wilson, A. M., Lowe, J. C., Roskilly, K., Hudson, P. E., Golabek, K. A., and McNutt, J. W., 2013, "Locomotion Dynamics of Hunting in Wild Cheetahs," *Nature*, **498**(7453), pp. 185–189.
- [2] Jusufi, A., Goldman, D. I., Revzen, S., and Full, R. J., 2008, "Active Tails Enhance Arboreal Acrobatics in Geckos," *Proc. Natl. Acad. Sci. U. S. A.*, **105**(11), pp. 4215–4219.
- [3] Walker, C., Vierck, C. J., Jr., and Ritz, L. A., 1998, "Balance in the Cat: Role of the Tail and Effects of Sacrocaudal Transection," *Behav. Brain Res.*, **91**(1–2), pp. 41–47.
- [4] O'Connor, S. M., Dawson, T. J., Kram, R., and Donelan, J. M., 2014, "The Kangaroo's Tail Propels and Powers Pentapedal Locomotion," *Biol. Lett.*, **10**, p. 20140381.
- [5] Mallison, H., 2010, "Cad Assessment of the Posture and Range of Motion of *Kentrosaurus Aethiopicus* Hennig 1915," *Swiss J. Geosci.*, **103**(2), pp. 211–233.
- [6] Saab, W., Rone, W. S., and Ben-Tzvi, P., 2017, "Robotic Modular Leg: Design, Analysis and Experimentation," *ASME J. Mech. Rob.*, **9**(2), p. 024501.
- [7] Saab, W., Rone, W. S., Kumar, A., and Ben-Tzvi, P., 2019, "Design and Integration of a Novel Spatial Articulated Robotic Tail," *IEEE Trans. Mechatronics* (in press).
- [8] Saab, W., Rone, W. S., and Ben-Tzvi, P., 2018, "Robotic Tails: A State of the Art Review," *Robotica*, **36**(9), pp. 1263–1277.
- [9] Patel, A., and Braae, M., 2014, "Rapid Acceleration and Braking: Inspirations From the Cheetah's Tail," IEEE International Conference on Robotics and Automation (ICRA), Hong Kong, China, May 31–June 7, pp. 793–799.
- [10] Chang-Siu, E., Libby, T., Tomizuka, M., and Full, R. J., 2011, "A Lizard-Inspired Active Tail Enables Rapid Maneuvers and Dynamic Stabilization in a Terrestrial Robot," IEEE/RSJ International Conference on Intelligent Robots and Systems, San Francisco, CA, Sept. 25–30, pp. 1887–1894.
- [11] Liu, G.-H., Lin, H.-Y., Lin, H.-Y., Chen, S.-T., and Lin, P.-C., 2014, "A Bio-Inspired Hopping Kangaroo Robot With an Active Tail," *J. Bionic Eng.*, **11**(4), pp. 541–555.
- [12] Berenguer, F. J., and Monasterio-Huelin, F. M., 2008, "Zappa, a Quasi-Passive Biped Walking Robot With a Tail: Modeling, Behavior, and Kinematic Estimation Using Accelerometers," *IEEE Trans. Ind. Electron.*, **55**(9), pp. 3281–3289.
- [13] Casarez, C., Penskiy, I., and Bergbreiter, S., 2013, "Using an Inertial Tail for Rapid Turns on a Miniature Legged Robot," IEEE International Conference on Robotics and Automation (ICRA), Karlsruhe, Germany, May 6–10, pp. 5469–5474.
- [14] Patel, A., and Braae, M., 2013, "Rapid Turning at High-Speed: Inspirations From the Cheetah's Tail," IEEE/RSJ International Conference on Intelligent Robots and Systems, Tokyo, Japan, Nov. 3–7, pp. 5506–5511.
- [15] Ikeda, F., and Toyama, S., 2015, "A Proposal of Right and Left Turning Mechanism for Quasi-Passive Walking Robot," IEEE International Conference on Advanced Robotics and Intelligent Systems (ARIS), Taipei, Taiwan, May 29–31.
- [16] Chang-Siu, E., Libby, T., Brown, M., Full, R. J., and Tomizuka, M., 2013, "A Nonlinear Feedback Controller for Aerial Self-Righting by a Tailed Robot," IEEE International Conference on Robotics and Automation (ICRA), Karlsruhe, Germany, May 6–10, pp. 32–39.
- [17] Mutka, A., Orsag, M., and Kovacic, Z., 2013, "Stabilizing a Quadruped Robot Locomotion Using a Two Degree of Freedom Tail," 21st Mediterranean Conference on Control and Automation, Chania, Greece, June 25–28, pp. 1336–1342.
- [18] Briggs, R., Lee, J., Haberland, M., and Kim, S., 2012, "Tails in Biomimetic Design: Analysis, Simulation, and Experiment," IEEE/RSJ International Conference on Intelligent Robots and Systems, Vilamoura, Portugal, Oct. 7–12, pp. 1473–1480.
- [19] Rone, W. S., Saab, W., and Ben-Tzvi, P., 2018, "Design, Modeling and Integration of a Flexible Universal Spatial Robotic Tail," *ASME J. Mech. Rob.*, **10**(4), p. 041001.
- [20] Rone, W. S., and Ben-Tzvi, P., 2017, "Design, Modeling and Optimization of the Universal-Spatial Robotic Tail," ASME Paper No. IMECE2017-71463.
- [21] Saab, W., Rone, W. S., and Ben-Tzvi, P., 2018, "Discrete Modular Serpentine Robotic Tail: Design, Analysis and Experimentation," *Robotica*, **36**(7), pp. 994–1018.
- [22] Rone, W. S., and Ben-Tzvi, P., 2016, "Dynamic Modeling and Simulation of a Yaw-Angle Quadruped Maneuvering With a Robotic Tail," *ASME J. Dyn. Syst. Meas. Control*, **138**(8), p. 084502.
- [23] Rone, W. S., and Ben-Tzvi, P., 2017, "Maneuvering and Stabilizing Control of a Quadrupedal Robot Using a Serpentine Robotic Tail," IEEE Conference on Control Technology and Applications (CCTA), Mauna Lani, HI, Aug. 27–30, pp. 1763–1768.
- [24] Godage, I. S., Branson, D. T., Guglielmino, E., Medrano-Cerda, G. A., and Caldwell, D. G., 2011, "Dynamics for Biomimetic Continuum Arms: A Modal Approach," IEEE International Conference on Robotics and Biomimetics, Phuket, Thailand, Dec. 7–11, pp. 104–109.
- [25] Hannan, M. W., and Walker, I. D., 2003, "Kinematics and the Implementation of an Elephant's Trunk Manipulator and Other Continuum Style Robots," *J. Rob. Syst.*, **20**(2), pp. 45–63.
- [26] Li, T., Nakajima, K., and Pfeifer, R., 2013, "Online Learning for Behavior Switching in a Soft Robotic Arm," IEEE International Conference on Robotics and Automation (ICRA), Karlsruhe, Germany, May 6–10, pp. 1296–1302.
- [27] Braganza, D., Dawson, D. M., Walker, I. D., and Nath, N., 2007, "A Neural Network Controller for Continuum Robots," *IEEE Trans. Rob.*, **23**(6), pp. 1270–1277.
- [28] Chitrakaran, V. K., Behal, A., Dawson, D. M., and Walker, I. D., 2007, "Setpoint Regulation of Continuum Robots Using a Fixed Camera," *Robotica*, **25**(5), pp. 581–586.
- [29] Camarillo, D. B., Carlson, C. R., and Salisbury, J. K., 2009, "Configuration Tracking for Continuum Manipulators With Coupled Tendon Drive," *IEEE Trans. Rob.*, **25**(4), pp. 798–808.
- [30] Bajo, A., Goldman, R. E., and Simaan, N., 2011, "Configuration and Joint Feedback for Enhanced Performance of Multi-Segment Continuum Robots," IEEE International Conference on Robotics and Automation (ICRA), Shanghai, China, May 9–13, pp. 2905–2912.
- [31] Gravagne, I. A., Rahn, C. D., and Walker, I. D., 2003, "Large Deflection Dynamics and Control for Planar Continuum Robots," *IEEE/ASME Trans. Mechatronics*, **8**(2), pp. 299–307.